

Time-dependent responses of the neutral mass density to magnetospheric energy inputs into the cusp region in the thermosphere: A high-resolution two-dimensional local modeling

Tomokazu Oigawa (✉ oigawa@kugi.kyoto-u.ac.jp)

Kyoto Daigaku <https://orcid.org/0000-0002-0985-303X>

Hiroyuki Shinagawa

National Institute of Information and Communications Technology Applied Electromagnetic Research Institute: Kokuritsu Kenkyu Kaihatsu Hojin Joho Tsushin Kenkyu Kiko Sogo Test Bed Kenkyu Kaihatsu Suishin Center Innovation Center

Satochi Taguchi

Kyoto University Graduate School of Science Faculty of Science: Kyoto Daigaku Rigaku Kenkyuka Rigakubu

Express Letter

Keywords: neutral mass density anomaly, neutral upwelling, cusp, Joule heating, neutral-ion drag

Posted Date: October 7th, 2020

DOI: <https://doi.org/10.21203/rs.3.rs-86164/v1>

License: © ⓘ This work is licensed under a Creative Commons Attribution 4.0 International License.

[Read Full License](#)

1 **Title page:**

2 **Time-dependent responses of the neutral mass density to magnetospheric energy**

3 **inputs into the cusp region in the thermosphere: A high-resolution two-dimensional**

4 **local modeling**

5 Author #1: Tomokazu Oigawa, Department of Geophysics, Graduate School of Science,

6 Kyoto University, Kyoto, Japan, oigawa@kugi.kyoto-u.ac.jp

7 Author #2: Hiroyuki Shinagawa, National Institute of Information and Communications

8 Technology, Tokyo, Japan, sinagawa@nict.go.jp

9 Author #3: Satoshi Taguchi, Department of Geophysics, Graduate School of Science,

10 Kyoto University, Kyoto, Japan, taguchi@kugi.kyoto-u.ac.jp

11 **Indicate the corresponding author: Correspondence Tomokazu Oigawa**

12

13 **Abstract**

14 Remarkable enhancements of the thermospheric mass density around the 400-km altitude
15 in the cusp region have been observed by the CHALLENGING Minisatellite Payload
16 (CHAMP) satellite. We employed a high-resolution two-dimensional local model to gain
17 insights into the extent to which the neutral-ion drag process controls the mass density's
18 enhancements under the energy inputs typical of the cusp. We expressed those energy
19 inputs by quasi-static electric fields and electron precipitation. We compared two cases
20 and calculated the thermospheric dynamics with and without neutral-ion drags. We found
21 that in the more realistic case containing the neutral-ion drag, the calculated mass density
22 enhancement was 10% at most, which is dramatically smaller than the observations by
23 the CHAMP satellite (33% on average). The results also showed that the neutral-ion drag
24 process suppresses Joule heating and neutral mass density enhancements, as well as the
25 chemical reaction process. The discrepancy between our modeling result and the satellite
26 observation suggests the existence of additional energy sources, such as Alfvén waves
27 propagating from the magnetosphere, which play an important role in the cusp's density
28 enhancement.

29
30 **Keywords:**

31 neutral mass density anomaly, neutral upwelling, cusp, Joule heating, neutral-ion drag

32

33 **Main Text**

34 **1. Introduction**

35 The cusp is typically located around 75° magnetic latitude between ~ 1000 and ~ 1400

36 magnetic local time in the altitudes of the ionosphere–thermosphere, where low energy

37 electrons almost directly come from the dayside magnetosheath. The ionosphere–

38 thermosphere dynamics in the cusp region are extremely complicated depending on

39 inputs from the dayside magnetosheath (e.g., solar wind particles and interplanetary

40 magnetic fields [IMFs]) and the condition of solar extreme ultraviolet (EUV) radiation.

41 Recent CHALLENGING Minisatellite Payload (CHAMP) satellite observations have shown

42 that the neutral mass density around the 400-km altitude in the cusp is remarkably larger

43 than that of ambient regions. After Lühr et al.'s (2004) discovery, the anomalous mass

44 density structure and other related phenomena have been extensively investigated in

45 observational and modeling studies. Kervalishvili and Lühr (2013) have shown that the

46 mass density enhancement is, on average, 33%.

47 The mass density anomaly is considered to be generated by thermospheric heating

48 processes, such as Joule heating and particle heating, which drive neutral upwelling.

49 Joule heating is caused by Pedersen currents depending on Pedersen conductivities,
50 perpendicular electric fields, and neutral winds. Electron precipitation enhances Pedersen
51 conductivity and, thus, Joule heating by ionization. In addition, electron precipitation
52 directly heats the neutral atmosphere.

53 Many modeling studies have been conducted to reproduce the mass density anomaly.
54 Under geomagnetically disturbed conditions, previous studies have partially been
55 successful in reproducing the mass density anomaly, while still facing difficulties in
56 reproducing sufficient mass density enhancements under quiet conditions. Crowley et al.
57 (2010) calculated mass density enhancements during strong IMF B_Y (+20 nT)
58 conditions and managed to generate mass density enhancements of over 200%. Wilder et
59 al. (2012) also employed the Thermosphere-Ionosphere-Mesosphere-Electrodynamics
60 General Circulation Model (TIME-GCM) (Roble et al. 1988; Roble and Ridley 1994) and
61 created a density change of over 100% for a geomagnetic storm. Drawing on Ridley et
62 al.'s (2006) Global Ionosphere–Thermosphere Model (GITM), Deng et al. (2013)
63 imposed an intense Poynting flux of 75 mW/m^2 and increased mass density by 60%.
64 Crowley et al. (2010), Wilder et al. (2012), and Deng et al. (2013) all assumed highly
65 strong disturbances. Brinkman et al. (2016), who used the Aerospace Dynamical Model
66 (ADM) (Walterscheid and Schubert 1990), obtained the result consistent with

67 observation as far as the model of moderate energy inputs is concerned. However, for the
68 strongest energy inputs arising from geomagnetic storms, their model's density
69 enhancements were well below the observations. Overall, the complete explanation of the
70 mass density anomaly for various conditions remains to be established.

71 Many previous studies have used global models such as TIME-GCM and GITM, which
72 have a horizontal resolution of around 100 km and a vertical resolution of one-half scale
73 height. However, the density anomaly has small-scale features, such as kilometer-scale
74 field-aligned currents and strong vertical dependencies of heating. Therefore, such global
75 models' spatial resolutions may be insufficient to describe the cusp's density structures.
76 Furthermore, the ion density, temperature, and velocity are highly variable, and these
77 high variabilities may considerably affect the neutral dynamics in the high-latitude
78 ionosphere. Thus, the precise calculations of spatially dependent and time-dependent ions'
79 profiles are crucial to the study of such ionosphere–thermosphere dynamics.

80 In this study, we investigated how ionospheric–thermospheric processes, such as Joule
81 heating, drag forces, and ion motion, contribute to the mass density anomaly by
82 developing a two-dimensional local model. We also examined the importance of
83 time-dependent features of ions for neutral dynamics. For this study, we compared two
84 cases: one with and another without neutral-ion drags.

85

86 **2. Model description**87 **2.1. Neutral dynamics**

88 We consider the neutrals to be composed of N_2 , O_2 , NO , N , O , and He . The continuity
89 equation of neutrals is

$$90 \frac{\partial n_j}{\partial t} + \nabla \cdot (n_j \mathbf{u}_n) = 0, (j = N_2, O_2, NO, N, O, He) \quad (1),$$

91 where n_j is the number density of neutral species j , and \mathbf{u}_n is the neutral flow velocity.

92 Including Coriolis force, pressure, collision to ions, gravity, and viscosity, the momentum
93 equation of neutrals can be written as

$$94 \frac{\partial \mathbf{u}_n}{\partial t} + (\mathbf{u}_n \cdot \nabla) \mathbf{u}_n + 2\boldsymbol{\Omega} \times \mathbf{u}_n = -\frac{1}{\rho_n} \nabla p_n - \nu_{ni} (\mathbf{u}_n - \mathbf{u}_i) + \mathbf{G} + \frac{1}{\rho_n} \nabla \cdot (\eta \nabla \mathbf{u}_n) \quad (2),$$

95 where $\boldsymbol{\Omega}$, ρ_n , p_n , ν_{ni} , \mathbf{G} , and η are the angular velocity of the Earth's rotation, the
96 neutral mass density, the neutral pressure, the neutral-ion collision frequency, the
97 gravitational acceleration, and the dynamic viscosity, respectively.

98 Considering adiabatic expansion, heat conduction, and external heating, the energy
99 equation of neutrals is given by

$$100 \frac{\partial T_n}{\partial t} + \mathbf{u}_n \cdot \nabla T_n = -\frac{RT_n}{c_v} \nabla \cdot \mathbf{u}_n + \frac{1}{\rho_n c_v} \nabla \cdot (\kappa \nabla T_n) + \frac{Q}{\rho_n c_v} \quad (3),$$

101 where T_n , R , c_v , κ , and Q are the neutral temperature, the specific gas constant, the
102 specific heat capacity at constant volume, the heat conductivity, and the volumetric

103 heating rate, respectively. In the auroral region, the external heat sources are mainly Joule
 104 heating and particle heating. The former Q_J is given by

$$105 \quad Q_J = \sigma_P (\mathbf{E} + \mathbf{u}_n \times \mathbf{B})^2 \quad (4),$$

106 where σ_P is the Pedersen conductivity. The latter Q_P will be described in 2.3.

107

108 **2.2. Ion dynamics**

109 We consider the ions to be composed of O_2^+ , N_2^+ , NO^+ , and O^+ . The continuity equation
 110 of ions is

$$111 \quad \frac{\partial n_k}{\partial t} + \nabla \cdot (n_k \mathbf{u}_i) = S_k, \quad (k = O_2^+, N_2^+, NO^+, O^+) \quad (5),$$

112 where S_k is the source term by ionization, recombination, and other chemical reactions.

113 This term will be described again in 2.3.

114 Assuming time derivative, advection, Coriolis force, and viscosity to be zero, the

115 momentum equation of ions is

$$116 \quad 0 = -\frac{1}{\rho_i} \nabla p_i + \frac{e}{m_i} (\mathbf{E} + \mathbf{u}_i \times \mathbf{B}) - \nu_{in} (\mathbf{u}_i - \mathbf{u}_n) + \mathbf{G} \quad (6),$$

117 where e is the elementary charge, and m_i is the mean molecular mass of ions.

118 In the perpendicular component of (6), Lorenz and collisional forces are dominant. Thus,

119 we can derive the perpendicular component of \mathbf{u}_i (i.e., $\mathbf{u}_{i\perp}$) as follows:

$$120 \quad \mathbf{u}_{i\perp} = \mathbf{u}_{n\perp} + \frac{k_i}{1+k_i^2} \frac{\mathbf{E} + \mathbf{u}_n \times \mathbf{B}}{B} + \frac{k_i^2}{1+k_i^2} \frac{(\mathbf{E} + \mathbf{u}_n \times \mathbf{B}) \times \mathbf{B}}{B^2} \quad (7),$$

121 where $k_i = \Omega_i/\nu_{in}$ ($\Omega_i = eB/m_i$ is the gyro frequency of ions).

122 The motion of ions to the parallel direction is determined by ambipolar diffusion.

123 Therefore, $\mathbf{u}_{i\parallel}$ is given by

$$124 \quad \mathbf{u}_{i\parallel} = \mathbf{u}_{n\parallel} - D_a \left[\frac{1}{n_i T_p} \nabla_{\parallel} (n_i T_p) + \frac{\sin I}{H_p} \frac{\mathbf{B}}{B} \right] \quad (8),$$

125 where

$$126 \quad T_p = \frac{T_e + T_i}{2}, \quad D_a = \frac{2k_B T_p}{m_i \nu_{in}}, \quad H_p = \frac{2k_B T_p}{m_i G} \quad (9).$$

127 T_p , D_a , and H_p are the plasma temperature, the ambipolar diffusion coefficient, and the

128 plasma scale height, respectively. T_e is the electron temperature, and T_i is the ion

129 temperature. I is the geomagnetic inclination, which is set to be 90° in this study for

130 convenience.

131 The ion temperature is approximated well by assuming a balance between the frictional

132 heating and the heat exchange with neutrals as follows (St.-Maurice and Hanson 1982):

$$133 \quad T_i = T_n + \frac{m_n}{3k_B} (\mathbf{u}_i - \mathbf{u}_n)^2 \quad (10).$$

134

135 **2.3. Electron precipitation**

136 To describe the effects of electron precipitation, we employed Fang et al.'s (2010)

137 empirical model, which derives the altitude profile of the total ionization rate due to

138 electron precipitation. We assumed the differential number flux of precipitating electrons

139 $\phi(U)$ as a kappa distribution as follows:

$$140 \quad \phi(U) = \frac{Q_0}{2U_0^3} \frac{(\kappa-1)(\kappa-2)}{\kappa^2} U \left(1 + \frac{U}{\kappa U_0}\right)^{-\kappa-1}, (\kappa = 4.97) \quad (11),$$

141 where Q_0 is the total energy flux, and U_0 is the characteristic energy. The peak altitude

142 of the ionization increases for lower characteristic energies. In the cusp region, the

143 electron precipitation is characterized by “soft” (~ 100 eV) electrons coming almost

144 directly from the magnetosheath.

145 Another effect of electron precipitation is particle heating. Precipitating electrons collide

146 with neutral molecules and transfer energy. Some energy is lost by dissociation and

147 radiation, and the rest eventually heats the molecules. Using the total ionization rate P

148 [$\text{m}^{-3}\text{s}^{-1}$], the particle heating rate Q_P [$\text{eV}/\text{m}^3\text{s}$] is given by

$$149 \quad Q_P = \Delta\epsilon P C_{eff} \quad (12),$$

150 where $\Delta\epsilon = 35$ eV is the mean ionization energy, and C_{eff} is the heating efficiency as

151 an empirical function of height (Rees et al. 1983; Richards 2013).

152

153 **2.4. Numerical implementation**

154 This study develops a new two-dimensional local model based on Shinagawa and

155 Oyama’s (2006) thermospheric neutral model. We set the x-axis, y-axis, and z-axis to be

156 directed eastwardly, northwardly, and upwardly. All physical quantities were assumed to

157 be uniform in the x-direction. The numerical domain ranged from 0 to 700 km in altitude
 158 and from $-3,000$ to $3,000$ km in meridional distance. We separate the domain into cells
 159 with a vertical size of $\Delta z = 5$ km and a horizontal size of $\Delta y = 10$ km. The time step Δt
 160 was set to be 1 ms. We employed the CIP (Cubic-Interpolated Pseudoparticle) method
 161 (Takewaki et al. 1985; Yabe et al. 1991; Yabe and Wang 1991) to obtain the time
 162 evolution. We set boundary conditions as follows: At $y = -3,000, 3,000$ km, $\partial f / \partial y = 0$
 163 for any physical quantity f . At $z = 0$ km, $\mathbf{u}_n = \mathbf{0}$, $\partial T_n / \partial z = 0$, and $\partial n_n / \partial z =$
 164 $\partial n_i / \partial z = 0$. At $z = 700$ km, $\partial \mathbf{u}_n / \partial z = \mathbf{0}$, $\partial T_n / \partial z = 0$, $\partial n_n / \partial z = -n_n / H_n$, and
 165 $\partial n_i / \partial z = -n_i / H_p$. The last two conditions mean diffusion equilibrium for neutrals and
 166 ions. The precipitating electron flux Q_0 and the northward electric field E_y were set to
 167 be Gaussian functions as follows:

$$168 \quad Q_0(y) = Q \exp \left[- \left(\frac{y}{W/2} \right)^2 \right], \quad E_y(y) = E \exp \left[- \left(\frac{y}{W/2} + \frac{1}{\sqrt{2}} \right)^2 \right] \quad (13),$$

169 where W is the scale width and set to be 200 km as a typical meridional width of the cusp.
 170 The peak of electron precipitation is located at the center ($y = 0$ km). The electric field
 171 peak was shifted from the center to the south to maximize the meridional gradient of E_y
 172 and, thus, the upward field-aligned current at the center. In this study, we set the peak
 173 electric field E to be 60 mV/m. Electron precipitation was imposed with total energy
 174 flux Q of 1.6 mW/m^2 and characteristic energy U_0 of 100 eV, which indicates “soft”

175 electrons into the cusp.

176 The initial condition of neutrals was set by the NRLMSISE-00 model (Picone et al. 2002)

177 with input parameters of $F_{10.7} = 100$ and $A_p = 10$. The ion profile was derived from the

178 IRI-2016 model (Bilitza et al. 2017). Since the original profile given by IRI-2016 was not

179 in equilibrium, we first ran the model for six hours without any external forcing. The

180 resulting ion profile was used as the initial condition in the following calculations.

181

182 **2.5. Modeling runs**

183 We performed three modeling runs to investigate the contributions of neutral-ion drags to

184 the neutral atmosphere. We calculated with neutral-ion drags in Case 1 and without them

185 in Case 2. Specifically, the collisional term of (2) $-v_{ni}(u_n - u_i)$ was dropped in Case 2.

186 All the modeling runs lasted 7,200 s (two hours).

187

188 **3. Results**

189 **3.1. Comparing the contributions of various ionospheric processes**

190 We define fractional density change as $\Delta\rho/\rho_0$, where ρ_0 is the initial neutral mass

191 density, and $\Delta\rho$ is the difference of neutral mass density from ρ_0 . Therefore, $\Delta\rho/\rho_0$

192 indicates the relative enhancement of mass density. For instance, $\Delta\rho/\rho_0 = 0.1$ means a

193 10% increase from the initial condition. Figure 1 shows the resulting north–south profiles
194 around the center at $t = 7,200$ s. The right side (positive values) of the horizontal axis is
195 the north. The contour maps in Figure 1a show the fractional density change, and vectors
196 show the neutral flow velocity. Figures 1b and 1c show the neutral temperature change
197 and specific heating rate, respectively. In altitudes of 200 to 400 km, the specific heating
198 rate is maximized, and then neutral air heats, which causes neutral upwelling and mass
199 density enhancements. Figure 1 shows that mass density enhancement, upward neutral
200 velocity, and the specific heating rate of Case 1 are all smaller than those in Case 2. The
201 peak values of mass density changes, neutral temperature changes, and vertical neutral
202 velocity are summarized in Table 1. The peak of mass density is located north from the
203 center in Case 1. When neutral-ion drags are present, the neutral air is pulled into the
204 direction of the $E \times B$ drift (westward). After that, the Coriolis force pulls the neutrals
205 northward, causing the large mass density in the northern region. The differences in peak
206 locations between the electric field and electron precipitation also cause weak
207 asymmetry.

208 Figure 2 shows the neutral atmosphere profiles at the 400-km altitude. Figures 2a, 2b, 2c,
209 and 2d show the mass density enhancements, temperature changes, northward velocity,
210 and upward velocity. Similar to Figure 1, the three neutral parameters in Case 1 are all

211 smaller than those in Case 2. The mass density in the north in Case 1 is larger than that in
212 the south. Figure 2c shows that the Coriolis force suppresses the southward flow in the
213 south region in Case 1. The peak values of the mass density changes at the 400-km
214 altitude are 9.5% in Case 1 and 12.1% in Case 2. Considering that CHAMP's mean mass
215 density enhancements are 33% (Kervalishvili and Lühr 2013), as mentioned above, the
216 peak values in our results are smaller than the observations. This will be discussed in
217 Section 4.

218

219 **3.2. Time evolution of neutral mass density and Joule heating rate**

220 Figure 3 shows the time evolution of mass density changes at the 400-km altitude and the
221 volumetric heating rate at the 300-km altitude, where Joule heating drives neutral
222 upwelling most effectively. Figure 3a shows that the neutral mass density oscillates until
223 about 50 min due to atmospheric gravity waves caused by sudden commencement of
224 heating at 0 min (in our calculations, electric fields and electron precipitation rise as step
225 functions at the beginning). After 50 min, the mass density increases very slowly in both
226 cases.

227 Figure 3b shows the time evolution of the volumetric heating rate. In both cases, Joule
228 heating initially increases by ionization and then decreases at several tens of minutes. The

229 volumetric heating rate at the 300-km altitude is initially 1.3 nW/m^3 and eventually
 230 grows to 2.0 nW/m^3 in Case 1 and 3.5 nW/m^3 in Case 2. In both cases, the Joule
 231 heating rate decreases with time, which is why mass density enhancements hardly enlarge
 232 for longer times of energy inputs. Although the difference between the two cases is not
 233 huge, the time-dependent ion-neutral coupling is important for calculating Joule heating
 234 and neutral mass density enhancements.

235

236 **4. Discussion**

237 **4.1. Effects of each process on the time evolution of Joule heating**

238 Figure 4 shows altitude profiles of the ion density, specific heating rate, ion temperature,
 239 and vertical ion velocity at the center at 40 and 120 min intervals in each case.

240 Assuming the $E \times B$ drift flow as the ion, the Joule heating rate (4) can be written as

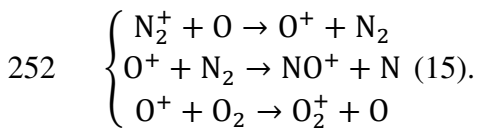
241 follows:

$$242 \quad Q_J = \sigma_p [(\mathbf{u}_n - \mathbf{u}_i) \times \mathbf{B}]^2 \quad (14).$$

243 Thus, larger velocity differences between neutrals and ions generate larger Joule heating
 244 rates. In Case 1, the horizontal neutral velocity is pulled into the $E \times B$ drift direction and
 245 finally reaches a value where the neutral-ion drag and viscous forces are balanced. (The
 246 Coriolis force is tiny in this direction.) Therefore, the neutral-ion drag reduces the Joule

247 heating, which is consistent with Billet et al.'s (2020) observations. Figures 4b and 4c
 248 show that both ion temperature and specific heating rate of Case 2 are larger than those of
 249 Case 1 since large velocity differences between neutrals and ions are maintained in Case
 250 2.

251 In the F layer, the major ion species is O^+ , and the dominant chemical reactions are



253 Neutral upwelling brings molecule-rich air to higher altitudes (Fuller-Rowell et al. 1996;
 254 Lu et al. 2016). Thus, the three chemical reactions above all act to decrease the O^+
 255 density in the F layer (Figure 4a). Figure 4d shows ion down-flow at 120 min,
 256 corresponding to the reduction of ions.

257 Both neutral-ion drags and chemical reactions in this model reduce Joule heating rates.

258 This result crucially indicates that the cusp's neutral mass density cannot be evaluated
 259 correctly in the fixed ionosphere condition.

260

261 **4.2. Comparison with previous studies**

262 Brinkman et al. (2016) have calculated mass density enhancements for various input
 263 parameters. Assuming that the electric field is $10 + 50$ mV/m (DC and AC components,
 264 respectively), the total energy flux is 1.6 mW/m², with a characteristic energy of 100 eV

265 and the cusp's meridional width of 2° , Brinkman et al. (2016) have shown that the
266 resulting mass density increase at the 400-km altitude is larger than 30%. In this
267 calculation, Brinkman et al. (2016) used fully ionized and fixed ionospheric profiles. In
268 contrast, our model solved ion density, temperature, and velocity dynamically, which
269 were not included in Brinkman et al.'s (2016) study. In our study with almost the same
270 conditions, the density increase was 10% in Case 1 and 12% in Case 2; a more realistic
271 model cannot reproduce larger density enhancements. This indicates that energy sources
272 other than those we considered crucial are needed to gain insights into the density
273 enhancements.

274 Previous studies have reported that electric field variability by Alfvén waves can play
275 important roles (Deng et al. 2009; Zhu et al. 2019). Since alternating electric fields keep
276 velocity differences between neutrals and ions large, the mass density's time evolution
277 may differ from what we presented above. Lotko and Zhang (2018) have shown that
278 Joule heating rates generated by Alfvén waves are maximized at F layer altitudes, with
279 the altitude profile depending on wavelength and frequency. In contrast, quasi-static
280 electric fields maximize Joule heating rates at E layer altitudes. We treated only
281 quasi-static electric fields in this study. Alfvén waves propagating from the
282 magnetosphere are candidates for the additional energy sources.

283 At present, we make a simple estimation of Alfvénic power to reproduce the observations.

284 Oscillating electric fields, on average, result in no horizontal ion motion. Thus, we can

285 estimate the average horizontal ion velocity $\mathbf{u}'_{i\perp}$ as follows:

$$286 \quad \mathbf{u}'_{i\perp} = \mathbf{u}_{n\perp} + \frac{k_i}{1+k_i^2} \frac{\mathbf{u}_n \times \mathbf{B}}{B} + \frac{k_i^2}{1+k_i^2} \frac{(\mathbf{u}_n \times \mathbf{B}) \times \mathbf{B}}{B^2} \quad (16).$$

287 We used $\mathbf{u}'_{i\perp}$ to calculate (2) and (5), but original $\mathbf{u}_{i\perp}$ was used in (10). Additionally,

288 the electric field peak was placed simply at the center rather than (13), since Alfvénic

289 fluctuations were excluded in large-scale field-aligned currents expressed by the

290 gradients of E_y in (13). In this estimation, the mass density enhancement at the 400-km

291 altitude became 31% when the electric field was 150 mV/m. This magnitude is too large

292 as a typical value of quasi-static electric fields but not an unrealistic value of Alfvén

293 waves amplitude. Swarm observations have shown that Alfvénic electric fields can

294 exceed 100 mV/m during moderately active conditions (Pakhotin et al. 2020). For an

295 in-depth discussion, it is essential to precisely calculate the height profile of Alfvénic

296 heating, which will be explored in our future works.

297

298 **5. Summary**

299 We used a high-resolution numerical model to investigate the neutral mass density's

300 time-dependent responses to magnetospheric energy inputs into the cusp region.

301 Contributions of neutral-ion drags were compared using two cases with and without
302 neutral-ion drags. Neutral-ion drag forces decrease velocity differences between neutrals
303 and ions. Chemical reactions reduce ions at *F* layer altitudes in response to neutral
304 upwelling. Both two processes suppress the Joule heating rate and mass density
305 enhancements. The mass density enhancement in the calculation containing the
306 neutral-ion drag process is 10% at most, which is remarkably smaller than the
307 observations by the CHAMP satellite (33% on average). This non-negligible discrepancy
308 indicates additional energy sources such as Alfvén waves propagating from the
309 magnetosphere, which play an important role in the cusp's density enhancement.

310

311 **Declarations**

312 **Ethics approval and consent to participate**

313 Not applicable.

314

315 **Consent for publication**

316 Not applicable.

317

318 **List of abbreviations**

319 IMF: interplanetary magnetic field

320 EUV: extreme ultra violet

321 MHD: magnetohydrodynamic

322

323 **Availability of data and materials**

324 The output data in this study can be provided on request to Tomokazu Oigawa.

325

326 **Competing interests**

327 The authors declare that they have no competing interests.

328

329 **Funding**

330 This work was supported by JSPS KAKENHI grant 15K05300.

331

332 **Authors' contributions**

333 TO implemented the simulation model, and prepared the manuscript. HS supervised its

334 implementation. ST designed the study. HS and ST edited the manuscript.

335

336 **Acknowledgments**

337 In this work we used the supercomputer of ACCMS, Kyoto University.

338

339 **References**

- 340 Billett D. D., Wild, J. A., Grocott, A., Aruliah, A. L., Ronksley, A. M., Walach, M.-T.,
 341 Lester, M. (2019). Spatially resolved neutral wind response times during high
 342 geomagnetic activity above Svalbard. *Journal of Geophysical Research: Space Physics*
 343 124, 6950–6960. doi: 10.1029/2019JA026627
- 344 Billett, D. D., Hosokawa, K., Grocott, A., Wild, J. A., Aruliah, A. L., Ogawa, Y., et al.
 345 (2020). Multi-instrument observations of ion-neutral coupling in the dayside cusp.
 346 *Geophysical Research Letters* 47, e2019GL085590. doi: 10.1029/2019GL085590
- 347 Brinkman, D. G., Walterscheid, R. L., Clemmons, J. H., Hecht, J. H. (2016).
 348 High-resolution modeling of the cusp density anomaly: Response to particle and Joule
 349 heating under typical conditions. *Journal of Geophysical Research: Space Physics* 121,
 350 2645-2661. doi: 10.1002/2015JA021658
- 351 Bilitza, D., Altadill, D., Truhlik, V., Shubin, V., Galkin, I., Reinisch, B., Huang, X.
 352 (2017). International Reference Ionosphere 2016: From ionospheric climate to real- time
 353 weather predictions. *Space Weather* 15, 418–429. doi: 10.1002/2016SW001593
- 354 Clemmons, J. H., Hecht, J. H., Salem, D. R., Strickland, D. J. (2008). Thermospheric
 355 density in the Earth’s magnetic cusp as observed by the Streak mission. *Geophysical*
 356 *Research Letters* 35, L24103. doi: 10.1029/2008GL035972
- 357 Crowley, G., Knipp, D. J., Drake, K. A., Lei, J., Sutton, E., Lühr, H. (2010).
 358 Thermospheric density enhancements in the dayside cusp region during strong B_Y
 359 conditions. *Geophysical Research Letters* 37, L07110. doi: 10.1029/2009GL042143
- 360 Deng, Y., Maute, A., Richmond, A. D., Roble, R. G. (2009). Impact of electric field
 361 variability on Joule heating and thermospheric temperature and density, *Geophysical*
 362 *Research Letters* 36, L08105. doi:10.1029/2008GL036916
- 363 Deng, Y., Fuller-Rowell, T. J., Akmaev, R. A., Ridley, A. J. (2011). Impact of the
 364 altitudinal Joule heating distribution on the thermosphere. *Journal of Geophysical*
 365 *Research* 116, A05313. doi: 10.1029/2010JA016019
- 366 Deng, Y., Fuller-Rowell, T. J., Ridley, A. J., Knipp, D., Lopez, R. E. (2013). Theoretical
 367 study: Influence of different energy sources on the cusp neutral density enhancement.
 368 *Journal of Geophysical Research: Space Physics* 118, 2340–2349. doi:
 369 10.1002/jgra.50197
- 370 Fang, X., Randall, C. E., Lummerzheim, D., Wang, W., Lu, G., Solomon, S. C., Frahm, R.
 371 A. (2010). Parameterization of monoenergetic electron impact ionization. *Geophysical*

- 372 Research Letters 37, L22106. doi: 10.1029/2010GL045406
- 373 Fuller- Rowell, T. J., Codrescu, M. V., Rishbeth, H., Moffett, R. J., Quegan,
374 S. (1996). On the seasonal response of the thermosphere and ionosphere to geomagnetic
375 storms, *Journal of Geophysical Research*, 101(A2), 2343– 2353. doi:
376 [10.1029/95JA01614](https://doi.org/10.1029/95JA01614)
- 377 Kervalishvili, G. N., & Lühr, H. (2013). The relationship of thermospheric density
378 anomaly with electron temperature, small-scale FAC, and ion up-flow in the cusp region,
379 observed by CHAMP and DMSP satellites. *Annales Geophysicae*, 31(3), 541–554. doi:
380 [10.5194/angeo-31-541-2013](https://doi.org/10.5194/angeo-31-541-2013)
- 381 Lotko, W., Zhang, B. (2018). Alfvénic heating in the cusp ionosphere-thermosphere.
382 *Journal of Geophysical Research: Space Physics* 123, 10,368–10,383. doi: 10.1029/
383 [2018JA025990](https://doi.org/2018JA025990)
- 384 Lu, G., Richmond, A. D., Lühr, H., Paxton, L. (2016). High-latitude energy input and its
385 impact on the thermosphere. *Journal of Geophysical Research: Space Physics* 121, 7108–
386 7124, doi: [10.1002/ 2015JA022294](https://doi.org/10.1002/2015JA022294)
- 387 Lühr, H., Rother, M., Köhler, W., Ritter, P., Grunwaldt, L. (2004). Thermospheric
388 upwelling in the cusp region: Evidence from CHAMP observations. *Geophysical*
389 *Research Letters* 31, L06805. doi: [10.1029/2003GL019314](https://doi.org/10.1029/2003GL019314)
- 390 Pakhotin, I. P., Mann, I. R., Knudsen, D. J., Lysak, R. L., Burchill, J. K. (2020).
391 Diagnosing the role of Alfvén waves in global field- aligned current system dynamics
392 during southward IMF: swarm observations. *Journal of Geophysical Research: Space*
393 *Physics* 125, e2019JA027277. doi: [10.1029/2019JA027277](https://doi.org/10.1029/2019JA027277)
- 394 Picone, J. M., Hedin, A. E., Drob, D. P., Aikin, A. C. (2002). NRLMSISE- 00 empirical
395 model of the atmosphere: Statistical comparisons and scientific issues. *Journal of*
396 *Geophysical Research* 107(A12), 1468. doi: [10.1029/2002JA009430](https://doi.org/10.1029/2002JA009430)
- 397 Rees, M. H., Emery, B. A., Roble, R. G., Stamnes, K. (1983), Neutral and ion gas heating
398 by auroral electron precipitation. *Journal of Geophysical Research* 88(A8), 6289– 6300.
399 doi: [10.1029/JA088iA08p06289](https://doi.org/10.1029/JA088iA08p06289)
- 400 Richards, P.G. (2013). Reevaluation of thermosphere heating by auroral electrons.
401 *Advances in Space Research* 51, 4, 610-619. doi: [10.1016/j.asr.2011.09.004](https://doi.org/10.1016/j.asr.2011.09.004)
- 402 Ridley, A. J., Deng Y., Toth, G. (2006). The global ionosphere-thermosphere model.
403 *Journal of Atmospheric and Solar-Terrestrial Physics*, 68, 839. doi:
404 [10.1016/j.jastp.2006.01.008](https://doi.org/10.1016/j.jastp.2006.01.008)
- 405 Roble, R. G., Ridley, E. C., Richmond, A. D., Dickinson, R. E. (1988). A coupled
406 thermosphere/ionosphere general circulation model. *Geophysical Research Letters* 15,
407 1325–1328. doi: [10.1029/GL015i012p01325](https://doi.org/10.1029/GL015i012p01325)

- 408 Roble, R. G. Ridley, E. C. (1994). Thermosphere-Ionosphere-Mesosphere-Electro
409 Dynamics General Circulation Model (TIME-GCM): Equinox solar cycle minimum
410 simulations (300– 500 km). *Geophysical Research Letters* 21, 417–420. doi:
411 10.1029/93GL03391
- 412 Rother, M., Schlegel, K., Lühr, H. (2007). CHAMP observation of intense
413 kilometer-scale field-aligned currents, evidence for an ionospheric Alfvén resonator.
414 *Annales Geophysicae* 25(7), 1603–1615. doi: 10.5194/angeo-25-1603-2007
- 415 Schlegel, K., Lühr, H., St.-Maurice, J.-P., Crowley, G., Hackert, C. (2005).
416 Thermospheric density structures over the polar regions observed with CHAMP. *Annales*
417 *Geophysicae* 23, 1659–1672. doi: 10.5194/angeo-23-1659-2005
- 418 St.- Maurice, J.- P., Hanson, W. B. (1982). Ion frictional heating at high latitudes and its
419 possible use for an in situ determination of neutral thermospheric winds and temperatures.
420 *Journal of Geophysical Research* 87(A9), 7580–7602. doi: 10.1029/JA087iA09p07580
- 421 Shinagawa, H., Oyama, S. (2006). A two-dimensional simulation of thermospheric
422 vertical winds in the vicinity of an auroral arc. *Earth, Planets and Space* 58,
423 1173-1181(2006). doi: 10.1186/BF03352007
- 424 Takewaki, H., Nishiguchi, A., Yabe, T. (1985). Cubic Interpolated Pseudopar- ticle
425 Method (CIP) for solving hyperbolic type equations. *Journal of Computational Physics*
426 61, 261–268. doi: 10.1016/0021-9991(85)90085-3
- 427 Thayer, J. P. (1998). Height- resolved Joule heating rates in the high- latitude *E* region
428 and the influence of neutral winds, *Journal of Geophysical Research* 103(A1) 471– 487.
429 doi: 10.1029/97JA02536
- 430 Walterscheid, R. L., Schubert, G. (1990). Nonlinear evolution of an upward propagating
431 gravity wave: Overturning, convection, transience, and turbulence. *Journal of the*
432 *Atmospheric Sciences* 47, 101–125. doi:
433 10.1175/1570-0469(1990)047<0101:NEOAUP>2.0.CO;2
- 434 Wilder, F. D., Crowley, G., Anderson, B. J., Richmond, A. D. (2012). Intense dayside
435 Joule heating during the 5 April 2010 geomagnetic storm recovery phase observed by
436 AMIE and AMPERE. *Journal of Geophysical Research* 117, A05207. doi:
437 10.1029/2011JA017262
- 438 Yabe, T., Wang, P. Y. (1991). Unified numerical procedure for compressible and
439 incompressible fluid. *Journal of the Physical Society of Japan* 60, 2105–2108. doi:
440 10.1143/JPSJ.60.2105
- 441 Yabe, T., Ishikawa, T., Wang, P. Y., Aoki, T., Kadota, Y., Ikeda, F. (1991). A
442 universal solver for hyperbolic equations by cubic-polynomial interpolation II. Two- and
443 three-dimensional solvers. *Computer Physics Communications* 66, 233–242. doi:

444 10.1016/0010-4655(91)90072-S

445 Zhu, Q., Deng, Y., Richmond, A., McGranaghan, R. M., Maute, A. (2019). Impacts of
446 multiscale FACs on the ionosphere- thermosphere system: GITM simulation. Journal of
447 Geophysical Research: Space Physics 124, 3532–3542. doi: 10.1029/2018JA026082

448

449 **Preparing illustrations and figures**

450 **Figure legends**

451 Figure 1

452 The resulting north–south profiles of the fractional density change and neutral velocity
453 (top), neutral temperature change (middle), and specific heating rate (bottom) in each
454 case. In the top, the contour maps show the fractional density change, and vectors show
455 the neutral flow velocity. The right side (positive values) of the horizontal axis is the
456 north. The peak of electron precipitation is located at the horizontal center.

457

458 Figure 2

459 The resulting profiles of the fractional density change (top), neutral temperature change
460 (middle top), northward neutral velocity (middle bottom), and vertical neutral velocity
461 (bottom) at the 400-km altitude in each case. Positive distance is directed to the
462 northward. The peak of electron precipitation is located at the center.

463

464 Figure 3

465 The time evolution of the fractional density change (top) and volumetric heating rate
466 (bottom) at the 400-km altitude in each case.

467

468 Figure 4

469 The resulting profiles of the ion density (left), specific heating rate (middle left), ion
470 temperature (middle right), and vertical ion velocity (right) at 40 min (top) and 120 min
471 (bottom) intervals in each case.

472

473 **Preparing tables**

474 Table 1 The resulting mass density enhancements, neutral temperature change, and
475 vertical neutral velocity

476

Figures

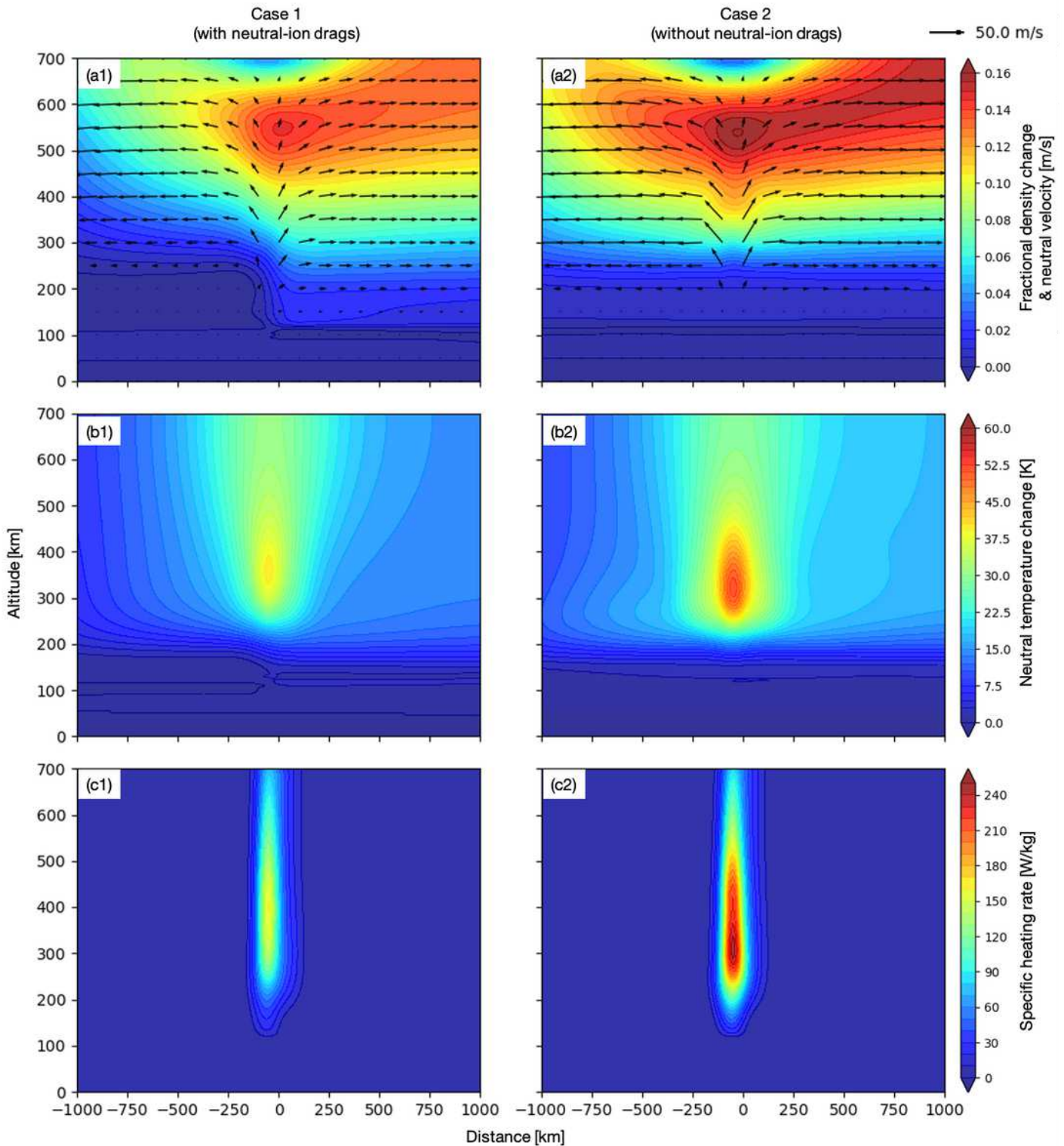


Figure 1

The resulting north-south profiles of the fractional density change and neutral velocity (top), neutral temperature change (middle), and specific heating rate (bottom) in each case. In the top, the contour maps show the fractional density change, and vectors show the neutral flow velocity. The right side

(positive values) of the horizontal axis is the north. The peak of electron precipitation is located at the horizontal center.

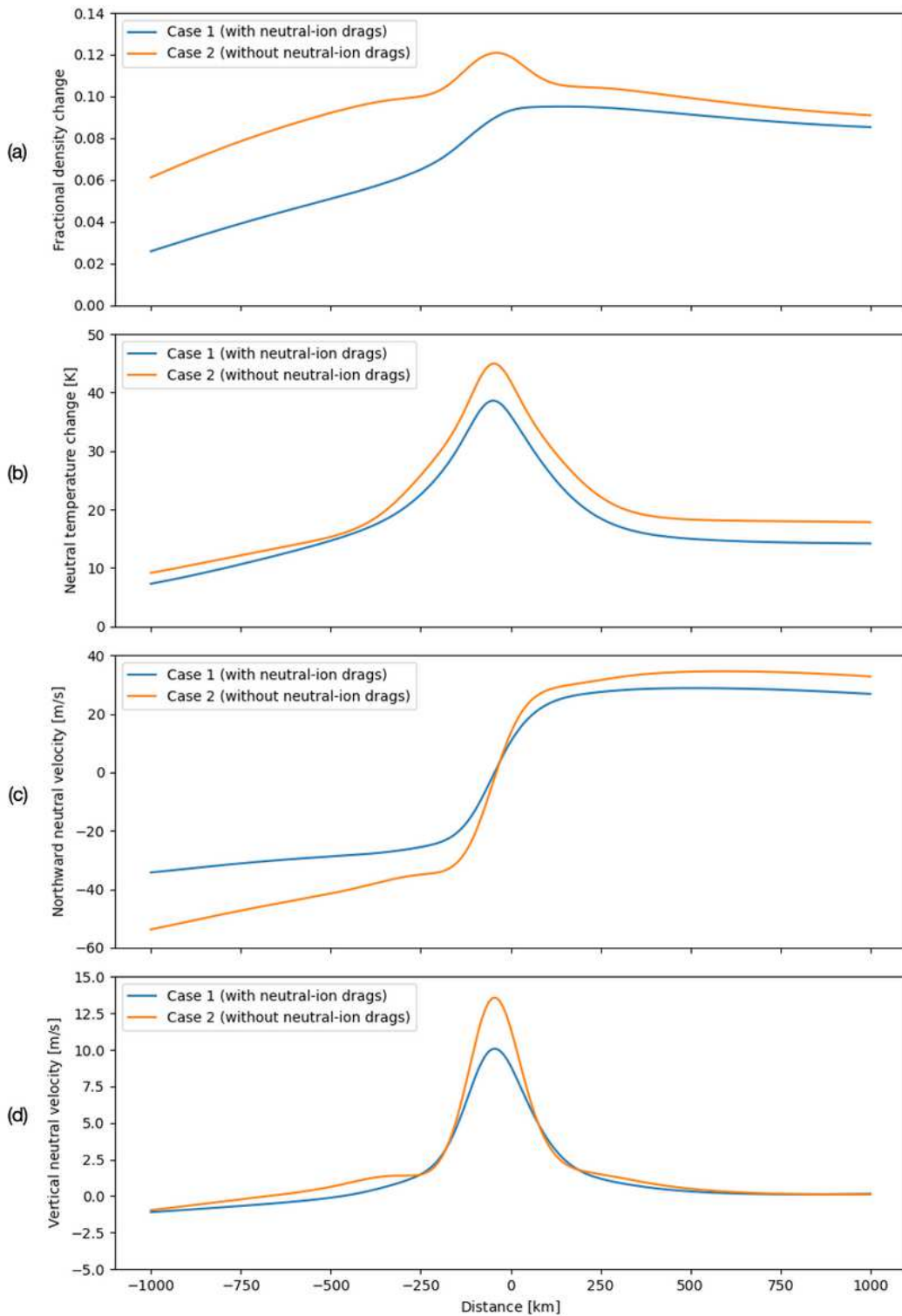


Figure 2

The resulting profiles of the fractional density change (top), neutral temperature change (middle top), northward neutral velocity (middle bottom), and vertical neutral velocity (bottom) at the 400-km altitude in

each case. Positive distance is directed to the northward. The peak of electron precipitation is located at the center.

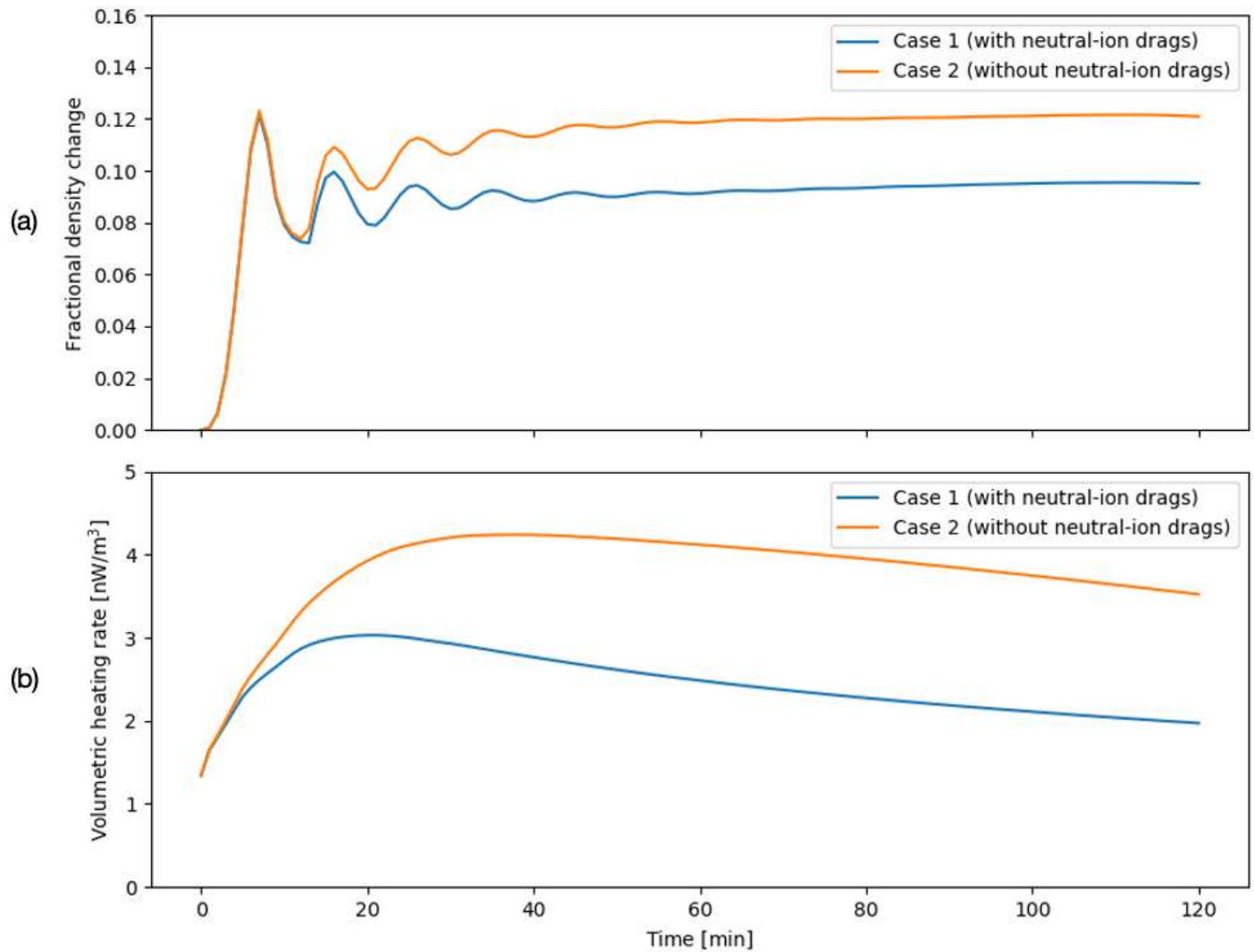


Figure 3

The time evolution of the fractional density change (top) and volumetric heating rate (bottom) at the 400-km altitude in each case.

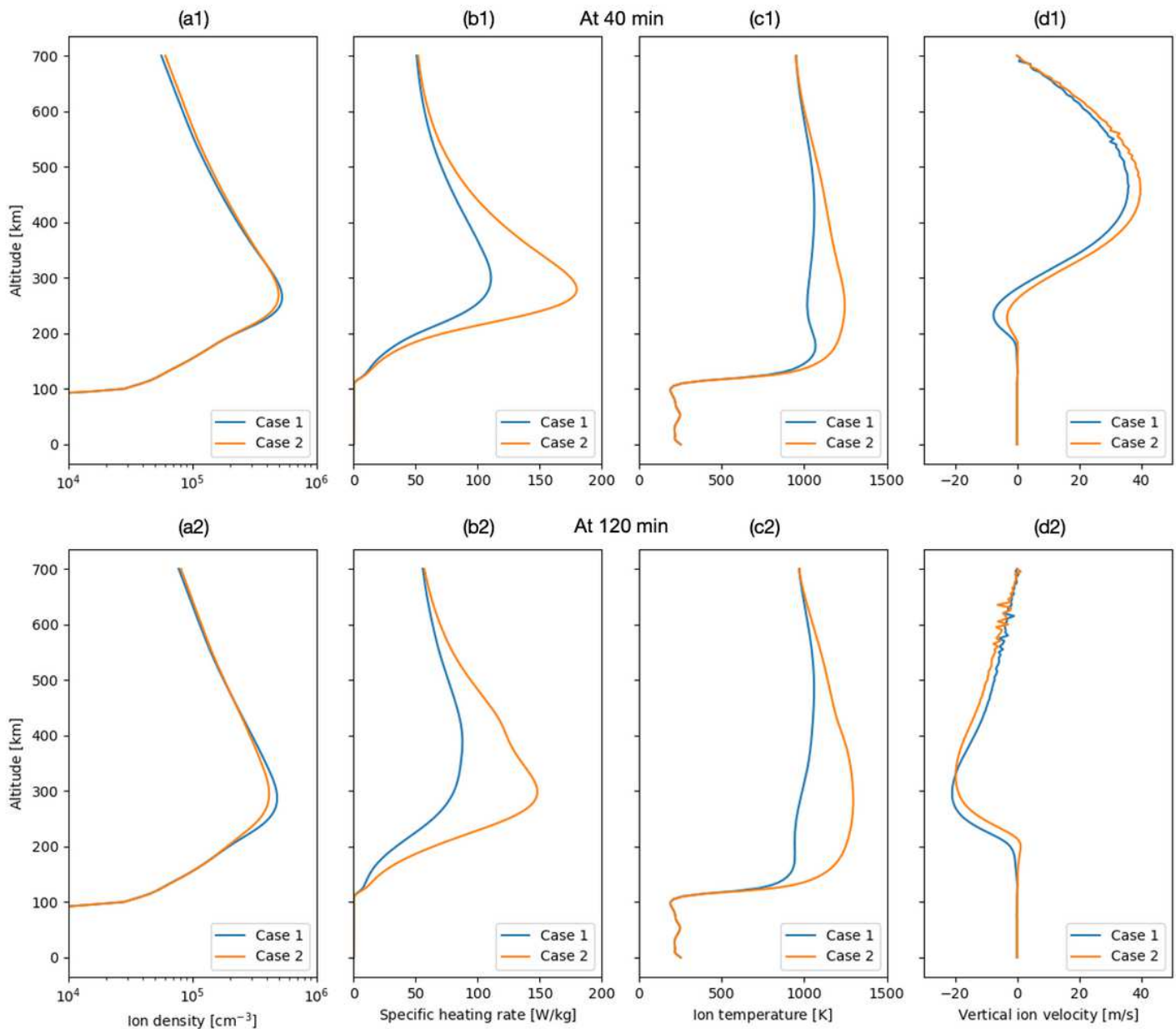


Figure 4

The resulting profiles of the ion density (left), specific heating rate (middle left), ion temperature (middle right), and vertical ion velocity (right) at 40 min (top) and 120 min (bottom) intervals in each case.

Supplementary Files

This is a list of supplementary files associated with this preprint. Click to download.

- [table1.xls](#)
- [graphicalabstract.png](#)